

# Nanoscale

Accepted Manuscript

This article can be cited before page numbers have been issued, to do this please use: A. Nexha, S. Mariani, A. Colbus, K. Cikalleshi, B. Mazzolai and T. Kraus, *Nanoscale*, 2026, DOI: 10.1039/D6NR00489J.



This is an Accepted Manuscript, which has been through the Royal Society of Chemistry peer review process and has been accepted for publication.

Accepted Manuscripts are published online shortly after acceptance, before technical editing, formatting and proof reading. Using this free service, authors can make their results available to the community, in citable form, before we publish the edited article. We will replace this Accepted Manuscript with the edited and formatted Advance Article as soon as it is available.

You can find more information about Accepted Manuscripts in the [Information for Authors](#).

Please note that technical editing may introduce minor changes to the text and/or graphics, which may alter content. The journal's standard [Terms & Conditions](#) and the [Ethical guidelines](#) still apply. In no event shall the Royal Society of Chemistry be held responsible for any errors or omissions in this Accepted Manuscript or any consequences arising from the use of any information it contains.

## ARTICLE

## Upconverting mixed emitter nanocomposites as sensitive luminescent thermometers within plant-inspired artificial fliers\*

Albenc Nexha,<sup>1</sup> Stefano Mariani,<sup>2</sup> Anja Colbus,<sup>1</sup> Kliton Cikalleshi,<sup>2,3</sup> Barbara Mazzolai,<sup>2\*</sup> and Tobias Kraus<sup>1,4\*</sup>Received 00th January 20xx,  
Accepted 00th January 20xx

DOI: 10.1039/x0xx00000x

The applicability of current upconverting lanthanide doped luminescent thermometers is limited by signal discriminability and thermal sensitivity. We overcome these limitations by creating fluorescent nanocomposites in biodegradable polyhydroxyalkanoates (PHA). Nanocomposites were designed that combine different lanthanide based upconverting nanoparticles. We create mixed emitter composites with bright red ( $\text{Mn}^{2+}$  doped with  $\text{Er}^{3+}$ ,  $\text{Yb}^{3+}$  in  $\text{NaYF}_4$ ), green ( $\text{Er}^{3+}$ ,  $\text{Yb}^{3+}$  in  $\text{BaYF}_5$ ) and blue ( $\text{Tm}^{3+}$ ,  $\text{Yb}^{3+}$  in  $\text{CaF}_2$ ) emitting particles to obtain clearly distinguishable and intense fluorescent signals. The resulting nanocomposites had maximum relative thermal sensitivities of 34%  $\text{K}^{-1}$ , outperforming existing thermometers. Importantly, their readout requires detection only in visible wavelength ranges, making them particularly suitable for drone-based environmental monitoring purposes. To demonstrate their applicability in this field, we integrate the nanocomposites into plant-inspired artificial fliers, creating self-deployable and biocompatible units for wireless monitoring of environmental temperature. The surface temperature of topsoil is reconstructed based on the fluorescence intensity ratio among the RGB (red-green-blue) wavelengths of the upconverting nanocomposites integrated into the fliers.

## Introduction

Upconverting lanthanide doped materials ( $\text{Ln}^{3+}$ ) can convert low energy near infrared (NIR) excitations into high energy emitting lights, spanning from ultraviolet (UV), visible (Vis) and NIR regions.<sup>1</sup> Their luminescent properties such as intensity, spectral position, bandwidth, band-shape, lifetime and polarization, are temperature-dependent, allowing for the application of these materials as luminescent thermometers.<sup>2,3</sup> These thermometers are able to detect temperature changes in a non-intrusive mode, combined with high accuracy, nanoscale spatial resolution and fast temporal response.<sup>2,3</sup> Due to these abilities,  $\text{Ln}^{3+}$  are continuously being investigated and developed for multiple applications ranging from biomedicine to photovoltaics.<sup>1-3</sup> Ongoing trials are devoted to the preparation of highly reliable and sensitive upconverting emitters.

The readout of such thermometers with band-shape or ratiometric techniques exploits the change of intensity ratios between two emission bands with temperature.<sup>2</sup> Ratiometric data is less affected by the optical setup, the concentration of the emitting ions and background signals from other emitters or light sources.<sup>2</sup> Most of existing ratiometric thermometers are based on thermally coupled levels (TCLs) of single emitting  $\text{Ln}^{3+}$  ions.<sup>2-4</sup> TCLs are closely spaced energy levels within an ion that

are in thermal equilibrium.<sup>2-4</sup> Their performance can be quantified using the relative thermal sensitivity ( $S_{rel}$ , in %  $\text{K}^{-1}$  units), a figure of merit that is independent of the characteristics of the materials (structural and morphological), operating wavelengths, or acquisition setups.<sup>2,3</sup>  $S_{rel}$  of TCL based thermometers is limited by the energy gap ( $\Delta E$ ) of the coupled levels, which is relatively small and in the range of 200  $\text{cm}^{-1}$  to 2000  $\text{cm}^{-1}$ .<sup>2-4</sup> For example, the thermometric performance of upconverting  $\text{Er}^{3+}$  doped materials based on the green TCL emissions  ${}^2\text{H}_{11/2}$  and  ${}^4\text{S}_{3/2}$  TCLs is generally below 1.5%  $\text{K}^{-1}$ .<sup>4</sup>  $\text{Tm}^{3+}$  or  $\text{Nd}^{3+}$  doped thermometers based on TCLs ( $\text{Tm}^{3+}$ :  ${}^3\text{F}_{2,3}$  and  ${}^3\text{H}_4$ , and  $\text{Nd}^{3+}$ : Stark sublevels of the  ${}^4\text{F}_{3/2}$  multiplet) exhibit sensitivities below 1%  $\text{K}^{-1}$ .<sup>2-4</sup> Furthermore, the small  $\Delta E$  of the emission can cause spectral overlap,<sup>5-7</sup> which makes detection harder and limits signal-to-noise ratios (SNR).

Dual emitting ions with opposite temperature dependent luminescent properties have been used to overcome these limitations in ratiometric sensing. For example, co-doping a host with  $\text{Eu}^{3+}$  and  $\text{Tb}^{3+}$  emitters can improve the SNR and the thermometric performance,<sup>8-10</sup> but only at cryogenic temperatures upon excitation with (phototoxic) UV light. Other thermometers based on  $\text{Ho}^{3+}$  and  $\text{Tm}^{3+}$  co-emitters are thermally stable and can be excited with NIR, but their maximum  $S_{rel}$  is around 2%  $\text{K}^{-1}$ .<sup>11,12</sup> Hybrid structures composed of quantum dots and  $\text{Ln}^{3+}$  have moderate  $S_{rel}$  in the range of 3%  $\text{K}^{-1}$ ,<sup>13,14</sup> but their performance is drastically hampered by the limited environmental stability of the quantum dots.<sup>3</sup> Therefore, the quest for thermometers with high sensitivities and easy readout is still ongoing.

Recently, strategies for integrating dual emitting  $\text{Ln}^{3+}$  that combine positive (decrease of intensity of the emission with

<sup>1</sup>INM-Leibniz Institute for New Materials, 66123 Saarbrücken, Germany<sup>2</sup>Bioinspired Soft Robotics Laboratory, Istituto Italiano di Tecnologia, Italy<sup>3</sup>The Biorobotics Institute, Scuola Superiore Sant'Anna, 56025 Pontedera, Italy<sup>4</sup>Saarland University, Colloid and Interface Chemistry, 66123 Saarbrücken, Germany

temperature, *i.e.* quench “off”) and negative (increase of intensity of emission with temperature, *i.e.* quench “on”) thermal quenching have been shown to boost thermometric performance.<sup>15</sup> Such thermometers combine two different hosts, for example  $\text{Er}^{3+}$  with green emission at 540 nm in  $\text{Er}^{3+}$ ,  $\text{Yb}^{3+}:\text{NaYF}_4@\text{NaYF}_4$  core@shell nanoparticles combined with  $\text{Tm}^{3+}:\text{Yb}_2\text{W}_3\text{O}_{12}$  particles where  $\text{Tm}^{3+}$  is emitting at 796 nm. The two emitters were integrated into hydrogels, and the combination of quench “off” ( $\text{Er}^{3+}$ , 540 nm) and quench “on” ( $\text{Tm}^{3+}$ , 796 nm) resulted in a maximum sensitivity up to 23.84%  $\text{K}^{-1}$  at 380 K.<sup>15</sup> Similar results were obtained when the 540 nm emission of  $\text{Er}^{3+}$  was combined with the emission of  $\text{Nd}^{3+}$  ions (at 799 nm within a  $\text{Nd}^{3+}:\text{Yb}_2\text{W}_3\text{O}_{12}$  matrix), with a sensitivity above 5%  $\text{K}^{-1}$  in the range from 350 K to 450 K, reaching a maximum of 15.3%  $\text{K}^{-1}$  at 380 K.<sup>15</sup> The  $\text{Yb}_2\text{W}_3\text{O}_{12}$  host has to be prepared by calcinating the precursors at 1273 K, resulting in microparticles with diameters of around 3  $\mu\text{m}$  and heterogeneous doping. The quench “on” mechanisms are sensitive to the concentration of the emitting ions, requiring extensive optimization for thermometry.<sup>15</sup> Finally, the readout of these thermometers required concurrent measurements in Vis and NIR regions. We are interested in upconverting emitters that enable thermometry with high sensitivities, can be combined in a modular fashion, and only require recording RGB (red-green-blue) wavelengths, so that the readout is possible with standard colour cameras.

Herein, we combine nanoparticles with positively thermally quenched levels of  $\text{Ln}^{3+}$  and embedded them into a polyhydroxyalkanoates (PHA) polymer matrix, a biodegradable and non-toxic polymer.<sup>16, 17</sup> Bright red ( $\text{Mn}^{2+}$  doped  $\text{Er}^{3+}$ ,  $\text{Yb}^{3+}$  in  $\text{NaYF}_4$ ), green ( $\text{Er}^{3+}$ ,  $\text{Yb}^{3+}$  in  $\text{BaYF}_5$ ) and blue ( $\text{Tm}^{3+}$ ,  $\text{Yb}^{3+}$  in  $\text{CaF}_2$ ) emitting nanoparticles are designed to prepare nanocomposites with high SNR, clearly distinguishable fluorescent signals and high  $S_{rel}$ . We use them as luminescent thermometers in plant-inspired artificial fliers, a class of 3D printed structures that mimic the properties of natural plant seeds,<sup>18, 19</sup> to monitor the temperature of topsoil. We 3D print artificial fliers inspired by natural *Acer campestre* seeds,<sup>18</sup> and integrate fluorescent nanocomposite build on the mixed emitters to monitor the surface temperature of topsoil within 268 K to 313 K.

## Experiments

### Chemicals and materials

All precursors were purchased from Sigma Aldrich. All chemicals were used without further purification. Polyhydroxyalkanoate (PHA) filaments were purchased from ColorFabb. Ethyl cyanoacrylate glue was purchased from Loctite, Henkel Corporation.

### Synthesis of upconverting nanoparticles

The upconverting particles were prepared via published solvothermal routes.<sup>20-22</sup> For the red emitting particles,<sup>21</sup> an aqueous dispersion (2.6 mL in total) containing  $\text{Mn}(\text{NO}_3)_2 \cdot 4\text{H}_2\text{O}$  (0.3 mmol),  $\text{Y}(\text{NO}_3)_3 \cdot 6\text{H}_2\text{O}$  (0.5 mmol),  $\text{Yb}(\text{NO}_3)_3 \cdot 5\text{H}_2\text{O}$  (0.18 mmol) and  $\text{Er}(\text{NO}_3)_3 \cdot 5\text{H}_2\text{O}$  (0.02 mmol) as added to a mixture of

oleic acid (16 mmol), NaOH (7.5 mmol) and distilled water (1.5 mL). After continuous stirring for 10 min, 4 mmol NaF in 2 mL distilled water were added dropwise to the mixture, followed by additional stirring for 30 min. The dispersion was transferred into a Teflon-lined autoclave reactor and heated at 200 °C for 8 h.

For the green emitting particles,<sup>20</sup> 0.5 mmol of an aqueous dispersion (1 mL in total) of rare earth nitrates (2 mol%  $\text{Er}(\text{NO}_3)_3 \cdot 5\text{H}_2\text{O}$ , 20 mol%  $\text{Yb}(\text{NO}_3)_3 \cdot 5\text{H}_2\text{O}$  and 78 mol%  $\text{Y}(\text{NO}_3)_3 \cdot 5\text{H}_2\text{O}$ ) and 0.5 mmol of an aqueous dispersion (3 mL in total) of  $\text{Ba}(\text{NO}_3)_2 \cdot 5\text{H}_2\text{O}$  were added to a vial containing oleic acid (64 mmol), ethanol (10 mL), NaOH (15 mmol) and distilled water (2 mL). After stirring for 10 minutes,  $\text{NH}_4\text{F}$  (4 mmol) dispersed in distilled water (1 mL) was added to the mixture. The mixture was transferred to a Teflon-lined autoclave reactor and heated at 210 °C for 24 h.

For the blue emitting particles,<sup>22</sup> aqueous solutions (1 mL in total) of 0.5 mmol of nitrate salts (0.5 mol%  $\text{Tm}(\text{NO}_3)_3 \cdot 5\text{H}_2\text{O}$ , 20 mol%  $\text{Yb}(\text{NO}_3)_3 \cdot 5\text{H}_2\text{O}$  and 78 mol%  $\text{Y}(\text{NO}_3)_3 \cdot 5\text{H}_2\text{O}$ ) and 2 mmol of NaF (in 4 mL distilled water) were added to a mixture of oleic acid (20 mL), ethanol (8 mL), NaOH (1.2 g) and deionized water (8 mL). The mixture was transferred to a Teflon-lined autoclave reactor and heated at 180 °C for 36 h.

The purification process was identical for all the upconverting particles. After the autoclave reactor had cooled down to room temperature, the nanoparticles were collected after washing several times with ethanol, followed by centrifugation and redispersion in organic solvents.

### Preparation of fluorescent composites

Fluorescent nanocomposites were prepared using a solvent evaporation process.<sup>18, 19</sup> Approximately 1 g of polyhydroxyalkanoates (PHA) polymer was dissolved in chloroform (approximately 10 mL) aided by vortex and ultrasound. Single emitting particles (blue, green and red) and mixed particles (blue/green, blue/red, and green/red) at different concentrations, were added to the PHA dispersion. After continuous stirring for approximately one hour, a uniformly dispersion was obtained. Then, around 2 mL of each composition was deposited into a Teflon template (circular shape, 10 cm in diameter). The solution was allowed to dry at room temperature to yield a fluorescent composite. Smaller disc-like composites with diameters of  $8.0 \pm 0.7$  mm were prepared using a Peddinghaus punch set.

### Characterizations of fluorescent materials and composites

Fluorescent nanocomposites were prepared using a solvent evaporation Transmission electron microscopy (TEM, JEOL JEM2100) operating at an acceleration voltage of 200 kV, was used to determine the size and shape of the upconverting nanoparticles. TEM specimens were prepared by depositing around 20  $\mu\text{L}$  of a diluted dispersion of the nanoparticles on the surface of a carbon-coated copper grid. The size of the nanoparticles was determined using ImageJ software after analyzing over 100 nanocrystals. Scanning electron microscopy (SEM) and energy dispersive X-ray spectroscopy (EDX) were



recorded using a Quanta 400ESEM (FEI Technologies Inc.) equipped with an EDX detector from Oxford Instruments. An acceleration voltage between 1 kV and 15 kV was used to acquire data. The crystalline structure of the fluorescent materials was characterized by X-ray powder diffraction (XRPD) using a D8 Advance diffractometer with a copper source  $\text{CuK}\alpha$  radiation ( $\lambda=1.54060 \text{ \AA}$ , 40 kV, 40 mA) with a  $2\theta$  range from  $10^\circ$ – $80^\circ$  and a scan rate of  $0.02^\circ$  per second. Raman spectroscopy was employed to characterize the vibrational modes of the fluorescent materials. A Renishaw inVia microscope with unpolarized light from a 532 nm argon laser, was focused on the materials by a 50x objective. Analysis was performed within the range of  $100\text{--}2000 \text{ cm}^{-1}$ , using a grating with 2400 lines/mm and an exposure time of 10 s. The photoluminescence of the fluorescent nanoparticles and nanocomposites was analysed by recording the emission spectra in a FS5 Edinburgh Instruments spectrofluorometer, equipped with an external 980 nm NIR laser source, placed perpendicular to the position of the fluorescent materials and composites. The emission spectra were acquired within the range from 400 nm to 800 nm with a resolution of 2 nm and an integration time of 0.5 s.

#### Production and characterizations of the fluorescent flying seeds

**Natural *Acer campestre* seed morphometric analysis.** The morphometric and aerodynamic features of the seeds were collected following the methodology outlined in earlier our research.<sup>18</sup> In summary, seeds of *Acer campestre* were gathered from a tree located in a rural area near Florence, Italy. Morphological measurements were obtained using a digital caliper (RS PRO 150 mm Digital Caliper) and a digital microscope (KH-8700). Seed mass was determined using an analytical balance (KERN ABS-N) with a sensitivity of  $\pm 0.0001 \text{ g}$ . These measurements were based on 10 distinct seeds. The morphological characteristics influencing flight performance included wing surface area ( $S$ ) and wing loading ( $W/S$ ). For these parameters, data was collected from 8 individual seeds. The wing surface area ( $S$ ) was derived from images of 10 *Acer campestre* seeds captured using the  $1280 \times 800$ -pixel camera of a Samsung A40 smartphone. Image analysis was carried out with ImageJ software,<sup>23</sup> where images were binarized, and  $S$  was estimated by counting black pixels within a known 2 cm scale bar.  $W/S$  was calculated using the measured seed weight ( $W$ ) and corresponding  $S$ .

**Determination of the indoor aerodynamic performance of the natural *Acer campestre* seeds.** The aerodynamic analysis of natural seeds under controlled laboratory conditions focused on quantifying key flight-related parameters, namely: descent speed ( $v_d$ ), rotational velocity ( $\Omega$ ), wing tip speed ( $v_t$ ), and conic angle ( $\beta$ ).<sup>24,25</sup> To assess  $v_d$ , *Acer campestre* seeds were released from a height of 2.95 meters in still air, ensuring no ventilation was present in the room. Their descent was captured using a Xiaomi Redmi Note 5 smartphone, featuring a  $1920 \times 1080$ -pixel resolution. The  $v_d$  was calculated by measuring the time interval from the moment of release to the moment the seed contacted the ground, as determined from video frames. Each

of the 10 seeds was dropped three times, resulting in a total of 30 trials. The same setup was adapted to determine  $\Omega$  and  $\beta$ . For this purpose, videos were recorded using an Apple iPhone 12 Pro Max at a frame rate of 240 fps (equivalent to 4.17 milliseconds between frames), with a resolution of  $1280 \times 800$  pixels. This procedure was also used to estimate  $\beta$ , which results from the interplay among centrifugal force acting on the distributed mass, gravitational force, and aerodynamic forces that induce torque about the flapping  $x$  axis.<sup>24,25</sup>

**Design of the artificial *Acer campestre* seeds.** The design of the artificial *Acer campestre* seed was based on a previously reported method.<sup>18</sup> Briefly, a top-view image of a natural *Acer campestre* samara was used in conjunction with the dimensional data previously reported.<sup>18</sup> The outline of the seed was traced and vectorized using Affinity Designer (trial version), and the resulting file was imported into Siemens NX, a 3D CAD modeling software, and scaled to develop the 2X artificial *Acer campestre* seed design. For manufacturing, a Fused Deposition Modeling (FDM) approach was used. The 3D model was exported in STL format and processed with Prusa Slicer. The internal infill density for pericarp of the seed was set to 15 %, and the print speed was adjusted to 20 mm/s. A Prusa i3 MKS printer was employed, using natural and biodegradable filament of polyhydroxyalkanoate (PHA) (ColorFabb). A nozzle with a 0.4 mm diameter was chosen. Compared to the previous biomimetic design,<sup>18</sup> we printed scaled versions of the artificial seed (twice, 2X) to allow for the placement of the fluorescent nanocomposites. The nanocomposites were attached to the pericarp of the printed artificial seeds using ethyl cyanoacrylate as a glue. The morphometric analysis and aerodynamic performance of artificial *Acer campestre* were estimated accordingly with the methods reported in “Natural *Acer campestre* seed morphometric analysis” and “Determination of the indoor aerodynamic performance of the natural *Acer campestre* seeds.”

#### Luminescent thermometry with fluorescent composites and artificial fliers

The performance of the upconverting nanocomposites was evaluated by monitoring the photoluminescence of the emitters as a function of temperature. The photoluminescence was recorded under identical conditions as for the nanoparticles, except that fluorescent composite discs were placed on a cooling/heating stage (Linkam Scientific Instruments, THMS 600) where surface temperature was additionally recorded using an infrared surface thermometer (IR 900 30-S from Voltcraft). Five photoluminescence spectra were recorded at each temperature.

A proof-of-concept experiment on monitoring the surface temperature of topsoil was performed in a custom-built optical setup. This setup consisted of a NIR laser operating at 980 nm wavelength (RLP-980-300 from Roithner Lasertechnik GmbH) focusing on the fluorescent nanocomposite attached to the



pericarp of the artificial flier, with a collimating lens (74-VIS from Ocean Optics) achieving a power density of  $0.4 \text{ W/cm}^2$ . The emitted fluorescence was collected using a  $400 \mu\text{m}$  diameter fiber (QP400-2-SRIBX from Ocean Optics) coupled with a high-resolution spectrometer (HB2000+ from Ocean Optics). The excitation light was removed using a  $750 \text{ nm}$  short pass dichroic filter (FESHO750 from Thorlabs). The NIR laser was aligned perpendicular to the seeds at approximately  $150 \text{ cm}$  distance. The fluorescence signal was collected by the fiber at an angle of  $60^\circ$  and a distance of  $20 \text{ cm}$  and entered the spectrometer where it was recorded with an integration time of  $10 \text{ s}$ . The artificial fliers were placed flat on the topsoil, and the intensity of the fluorescence was recorded as a function of the temperature of the soil during 12 hours within a laboratory. The temperature of the soil surface was monitored separately using the IR 900 30-S infrared thermometer.

## Results and Discussion

Upconverting nanoparticles with lanthanide ions ( $\text{Er}^{3+}$ ,  $\text{Tm}^{3+}$  and  $\text{Yb}^{3+}$ ) doped in tetragonal  $\text{BaYF}_5$ , cubic  $\text{NaYF}_4$ , and cubic  $\text{CaF}_2$  hosts were synthesized via solvothermal protocols.<sup>20-22</sup> The nanoparticles were coated with oleic acid and dispersed in organic solvents. We ensured that they had high crystallinity and low phonon energies (Fig. S1, SI), prerequisites for reduction of non-radiative processes, and promotion of radiative processes for bright photoluminescence of the emitting lanthanide ions.<sup>1</sup> The diffraction patterns of the hosts indicate minor crystalline impurities (Fig. S1, SI) as is commonly reported for this route.<sup>20,21</sup> The morphology of the particles was determined from transmission electron micrographs (TEM), revealing rectangular-like shapes with maximal dimensions of  $27 \pm 5 \text{ nm}$  for  $\text{BaYF}_5$  (Fig. 1A), square-like shape with  $17 \pm 3 \text{ nm}$  for  $\text{NaYF}_4$  (Fig. 1B), and spherical particles with diameters of  $10 \pm 2 \text{ nm}$  for the  $\text{CaF}_2$  host (Fig. 1C).

Upconversion of the nanoparticles was triggered with a  $980 \text{ nm}$  NIR laser. All nanoparticles displayed the characteristic emission spectra of  $\text{Er}^{3+}$  and  $\text{Tm}^{3+}$ .<sup>1</sup> Doping  $\text{Er}^{3+}$ ,  $\text{Yb}^{3+}$  into tetragonal  $\text{BaYF}_5$  generated bright green emissions with two typical bands located at  $520 \text{ nm}$  and  $540 \text{ nm}$  (Fig. 1D). When these two ions were doped together with  $\text{Mn}^{2+}$  into a cubic  $\text{NaYF}_4$  host,<sup>19</sup> a bright red emission became dominant (Fig. 1E).  $\text{Mn}^{2+}$  ions guide the formation of the cubic phase of  $\text{NaYF}_4$  host, in addition to promoting a dominant red emission instead of the usual green emissions of  $\text{Er}^{3+}$ .<sup>19</sup> Co-doping  $\text{Tm}^{3+}$  with  $\text{Yb}^{3+}$  into a cubic  $\text{CaF}_2$  host led to the typical blue emissions (Fig. 1F).

In all of these upconverting materials,  $\text{Yb}^{3+}$  ion acts as sensitizer by absorbing the  $980 \text{ nm}$  irradiation that populates the energy levels of the activators ( $\text{Er}^{3+}$  and  $\text{Tm}^{3+}$ ) via energy transfer (ET). Within these energy levels, the electrons populate high-lying levels of the activators ( $^4\text{F}_{7/2}$  for  $\text{Er}^{3+}$  and  $^1\text{D}_2$  for  $\text{Tm}^{3+}$ ), followed by non-radiative relaxations to low-lying levels or radiative relaxation to ground states that causes the

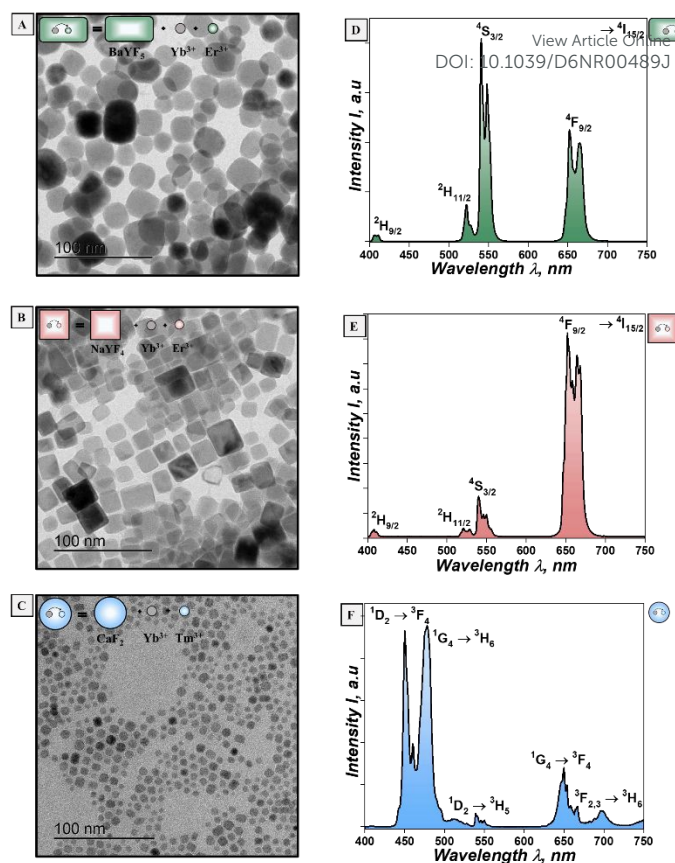


**Fig. 1** Transmission electron micrographs (TEM) and photoluminescence spectra of the upconverting nanoparticles emitting at (A), (D) green ( $\text{Er}^{3+}$ ,  $\text{Yb}^{3+}$ : $\text{BaYF}_5$ , drawn as a green rectangle), (B), (E) red ( $\text{Mn}^{2+}$ ,  $\text{Er}^{3+}$ ,  $\text{Yb}^{3+}$ : $\text{NaYF}_4$ , drawn as a red square), and (C), (F) blue ( $\text{Tm}^{3+}$ ,  $\text{Yb}^{3+}$ : $\text{CaF}_2$ , drawn as a blue sphere) wavelengths after excitation at  $980 \text{ nm}$  wavelength.

characteristic visible emissions in the blue (for  $\text{Tm}^{3+}$ ), or green and red (for  $\text{Er}^{3+}$ ).<sup>1,2</sup>

For the green and red emissions of  $\text{Er}^{3+}$ , non-radiative decays from  $^4\text{F}_{7/2}$  can populate  $^2\text{H}_{11/2}$ ,  $^4\text{S}_{3/2}$  and  $^4\text{F}_{9/2}$  before decaying radiatively to the ground state  $^4\text{I}_{15/2}$  level, which generates the bands at  $520 \text{ nm}$ ,  $540 \text{ nm}$  and  $660 \text{ nm}$ , respectively. For the blue emissions of  $\text{Tm}^{3+}$ , a direct radiative transition from  $^1\text{D}_2 \rightarrow ^3\text{F}_4$  level generates the emission at  $450 \text{ nm}$ , while non-radiative transitions that populate  $^1\text{G}_4$  enable radiative transition to  $^3\text{H}_6$  that generates the Stark bands at  $460 \text{ nm}$  and  $475 \text{ nm}$ .

Fluorescent nanocomposites were first prepared by combining the nanoparticles with a polymer matrix using a solvent evaporation process.<sup>18, 19</sup> Polyhydroxyalkanoate (PHA) was selected as matrix polymer due to its biodegradability, non-toxicity and renewable properties.<sup>16, 17</sup> PHA is synthesized through the fermentation of renewable feed stocks like sugars or plant oils.<sup>16, 17</sup> The polymer was dissolved in chloroform and the solution mixed with nanoparticle powders (e.g. red emitting  $\text{Mn}^{2+}$ ,  $\text{Er}^{3+}$ ,  $\text{Yb}^{3+}$  in  $\text{NaYF}_4$  host) at different concentrations ( $1\text{--}20 \text{ wt}\%$ ). The dispersions were drop casted on a Teflon substrate and dried. We created circular composites of  $8.0 \pm 0.7 \text{ mm}$  in diameter with thicknesses of  $200 \pm 25 \mu\text{m}$  and a mass of  $3.3 \pm 1.0 \text{ mg}$  (Fig. 2A).



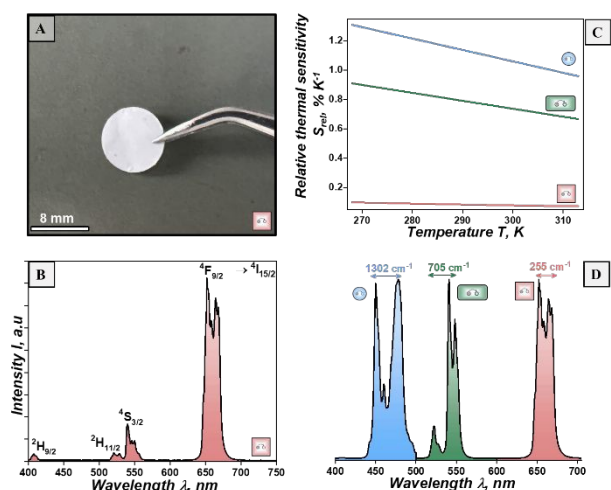


**Fig. 2** Fluorescent single emitter nanocomposites with PHA matrices filled with different types of upconverting nanoparticles. (A) Photograph and (B) upconversion spectra of the fluorescent nanocomposites based on red emitting nanoparticles ( $\text{Mn}^{2+}$ ,  $\text{Er}^{3+}$ ,  $\text{Yb}^{3+}$ : $\text{NaYF}_4$ ). (C)  $S_{rel}$  and (D) Illustration of TCLs and  $\Delta E$  of the blue ( $\text{Er}^{3+}$ ,  $\text{Tm}^{3+}$ : $\text{CaF}_2$ ), green ( $\text{Er}^{3+}$ ,  $\text{Yb}^{3+}$ : $\text{BaYF}_5$ ) and red ( $\text{Mn}^{2+}$ ,  $\text{Er}^{3+}$ ,  $\text{Yb}^{3+}$ : $\text{NaYF}_4$ ) emitters used for the calculation of  $S_{rel}$  in (C).

Nanoparticle filling ratios were optimized to produce a mechanically stable nanocomposite. Excessive filling ratios led to brittle materials and deformation during drying (Fig. S2, SI). We found that 15 wt% nanoparticles resulted in suitable composites (Fig. 2A) with uniform distribution of the particles within the matrix (as confirmed from SEM and EDX data, Fig. S2, SI) and adequate intensity levels of the upconverting emissions (Fig. 2B, and Fig. S2, SI). Higher concentrations likely caused agglomeration and heterogeneous packing.

The photostability of the fluorescent nanocomposites was experimentally evaluated. Lanthanide doped materials are known to exhibit self-heating upon laser irradiation at 980 nm, which we wanted to exclude.<sup>1-3</sup> We continuously irradiated the fluorescent nanocomposites with 980 nm laser operating at a power density of 0.4 W/cm<sup>2</sup>, a value reported to avoid self-heating in upconverting materials.<sup>1-3</sup> The intensities of the emissions at 475 nm, 540 nm and 660 nm for the blue, green and red nanocomposites, respectively, were recorded during 30 h (Fig. S3, SI). After 30 h, the intensities of the green, red and blue single emitters had dropped by approximately by 0.8%, 0.3% and 0.5% of their respective original values. These data suggest that the overall composite structure is virtually unaffected by the NIR irradiation at this power density, and 0.4 W/cm<sup>2</sup> was used in all later measurements.

The thermometric performance of the fluorescent composites was determined using  $S_{rel}$  that indicates the maximum change of the thermometric parameter ( $\Delta$ ) per degree of temperature change and is calculated as follows:<sup>2, 3</sup>

$$S_{rel} = \frac{1}{\Delta} \left| \frac{\partial \Delta}{\partial T} \right| \cdot 100\% \quad (1)$$

The thermometric parameter is defined as:<sup>2, 3</sup>

$$\Delta = \frac{I_1}{I_2} \quad (2)$$

where  $I_1$  and  $I_2$  are the integrated areas of the two emissions used for thermometry. For the TLC based emitters,  $\Delta$  depends on  $\Delta E$  of the emitting levels as:<sup>2, 3</sup>

$$\Delta = \frac{I_1}{I_2} = B \cdot \exp\left(-\frac{\Delta E}{k_B T}\right) \quad (3)$$

where  $k_B$  is Boltzmann's constant,  $T$  is the temperature, and  $B$  an experimental parameter usually determined from the fitting of the experimental data. Section S1 in the SI describes the fitting data and equations to determine  $S_{rel}$  in detail.

The thermometric performance of our single emitter nanocomposites was investigated from 268 K to 313 K. For the green emitting composites,  $S_{rel}$  depends on the ratio of two TCLs centred at 520 nm and 540 nm (Fig. S4, SI). For the red emitting composites, the Stark sublevels centred at 650 nm to 660 nm were used to calculate  $S_{rel}$  (Fig. S4, SI). For the blue emitting composites,  $S_{rel}$  was based on the  $\Delta$  calculated from the integral intensities centred at 450 nm and 475 nm (Fig. S4, SI). All three nanocomposites displayed relatively low  $S_{rel}$  below 1.5% K<sup>-1</sup> (Fig. 2C). As expected,  $S_{rel}$  decreased with increasing the operating temperatures (Equation S3, Section I, SI) and was proportional to and limited by the  $\Delta E$  between the two emission bands used for sensing (Equation S3, Section I, SI), i.e. 705 cm<sup>-1</sup>, 255 cm<sup>-1</sup> and 1302 cm<sup>-1</sup> for green, red and blue composites, respectively (Fig. 2D). The small spectral gaps (Stark sublevels on the red composites) or the overlaps (for the blue composites) between the emissions used in sensing limited the

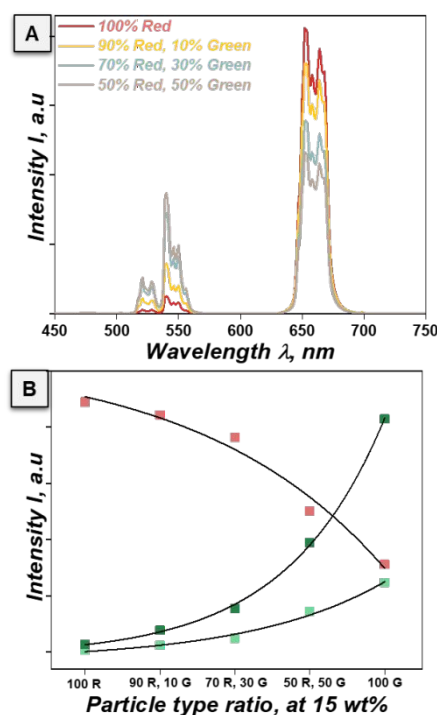


**Fig. 3** Mixed emitter nanocomposites for sensitive thermometry with RGB readout. (A) Upconversion spectra and (B) intensities of the 520 nm (light green color), 540 nm (dark green color), and 650 nm (red color) bands of PHA composites containing combinations of red  $\text{Mn}^{2+}$  doped  $\text{Er}^{3+}$ ,  $\text{Yb}^{3+}$ : $\text{NaYF}_4$  ("R" for "Red") and green  $\text{Er}^{3+}$ ,  $\text{Yb}^{3+}$ : $\text{BaYF}_5$  ("G" for "Green") nanoparticles as a function of filler fraction at a constant overall 15 wt% filling ratio. All samples were excited with a 980 nm laser operating at 0.4 W/cm<sup>2</sup>.

discriminability and thus, the achievable accuracy.



In the following, we introduce a strategy based on nanocomposites with mixed emitters that avoids spectral overlap and provides more freedom to combine emissions for improved  $S_{rel}$ . Upconverting nanoparticles with emissions at blue, green and red wavelengths were combined to provide easily distinguishable emissions and significantly improve SNR. This enabled sensitive thermometers with temperature dependent upconversion spectra that can be tailored to the application. For example, the green and the blue emitters are quenched with temperature, while the red emitters are barely influenced (Section I, SI), because they are not thermally coupled. The small temperature dependence likely is due to multiphonon relaxation pathways that populate the  $^4F_{9/2}$  level, which are weakly affected by temperature.<sup>21</sup> Our mixed emitter nanocomposites exploit these differences to boost thermometric performance.

nearly 14-fold that the green band (520 nm to 570 nm) (labelled as "100% Red", red line, Fig. 3A). We increased the fraction of

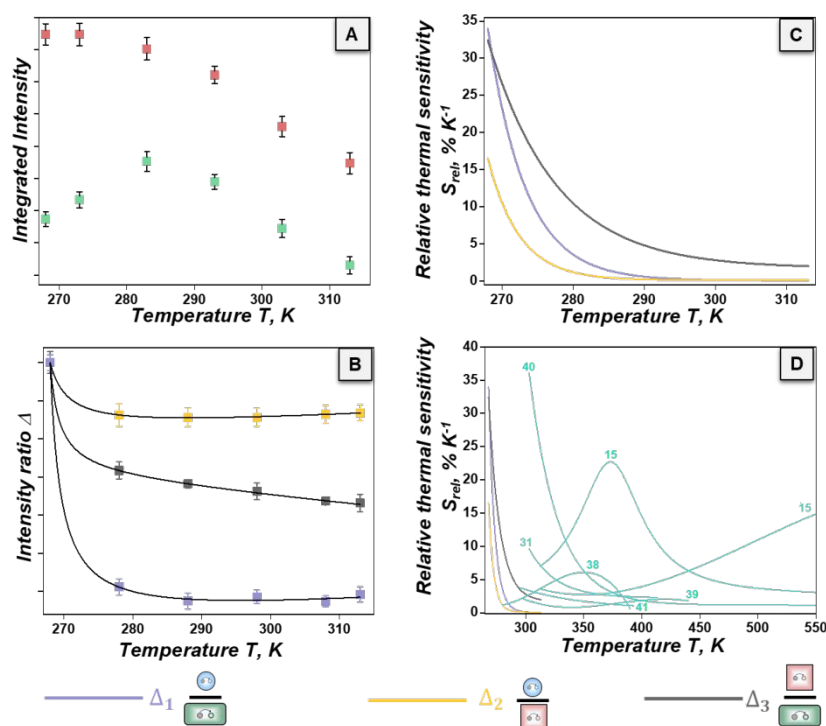


**Fig. 4** Thermometric performance of mixed emitter nanocomposites: (A) integrated intensities of the green (520 nm to 570 nm, in green) and red (620 nm to 680 nm, in red) emissions from green/red mixed composites as an example (cf. SI for all other wavelengths), (B) intensity ratios  $\Delta_i$  (symbols are experimental data, the solid line is the polynomial fit with Equation 4) and (C)  $S_{rel,j}$  as a function of temperature. (D) Comparison of state of the art  $S_{rel}$  of thermometers based on NTCLs (blue lines) with our mixed emitters. Numbers indicate the references containing the respective  $S_{rel}$  values.

overlap and provides more freedom to combine emissions for improved  $S_{rel}$ . Upconverting nanoparticles with emissions at blue, green and red wavelengths were combined to provide easily distinguishable emissions and significantly improve SNR. This enabled sensitive thermometers with temperature dependent upconversion spectra that can be tailored to the application. For example, the green and the blue emitters are quenched with temperature, while the red emitters are barely influenced (Section I, SI), because they are not thermally coupled. The small temperature dependence likely is due to multiphonon relaxation pathways that populate the  $^4F_{9/2}$  level, which are weakly affected by temperature.<sup>21</sup> Our mixed emitter nanocomposites exploit these differences to boost thermometric performance.

We prepared mixed emitter nanocomposites using the same solvent evaporating process as for the single emitters. The fractions of each emitter type were varied at the optimal overall filling ratio of 15 wt% established above and optimized to create mixed nanocomposites with RGB emissions at equivalent intensity levels. Fig. 3 shows a mixed emitter nanocomposite with red ( $Mn^{2+}$ ,  $Er^{3+}$ ,  $Yb^{3+}$ :NaYF<sub>4</sub>) and green ( $Er^{3+}$ ,  $Yb^{3+}$ :BaYF<sub>5</sub>) emitters as an example. The single emitter red composite with 15 wt%  $Mn^{2+}$ ,  $Er^{3+}$ ,  $Yb^{3+}$ :NaYF<sub>4</sub> nanoparticles had an emission in the red band (620 nm to 680 nm) with an intensity that was

the green emitters in the mixed emitter composite ( $Er^{3+}$ ,  $Yb^{3+}$ :BaYF<sub>5</sub>) in three steps to adjust the relative intensities and chose equal fractions of the emitters to obtain the final mixed emitter with aligned band intensities (Fig. 3A). The same adjustments were performed in blue/green and blue/red mixed emitter nanocomposites (Fig. S5, SI). The low quantum yield of the blue emitting composites required a 9-fold higher concentration in comparison to the red or green emitters in the respective mixtures (Fig. S5, SI).

Next, we discuss the origin of the overall emission from our mixed emitter nanocomposites. Direct non-radiative energy exchange between the nanoparticles do not occur at particles distances above 5 nm. However, spectral overlaps exist that explain why the overall emission of the mixed emitter nanocomposites is not a linear superposition of the individual particles (Fig. 3B). The green emissions of  $Er^{3+}$  can be triggered by the emissions from  $Tm^{3+}$  via radiative re-absorption. Emissions from  $Tm^{3+}$  in  $Tm^{3+}$ ,  $Yb^{3+}$ :CaF<sub>2</sub> in the UV (340 to 380 nm), blue (450 to 500 nm), red (650 to 670 nm), and NIR (at 800 nm) (Fig. S6, SI) may overlap with  $Er^{3+}$  absorption bands in the UV (300 to 400 nm), blue (400 to 500 nm), and NIR (800 nm, 980 nm and 1520 nm).<sup>26-29</sup> We would thus expect that some emissions from  $Tm^{3+}$  is absorbed



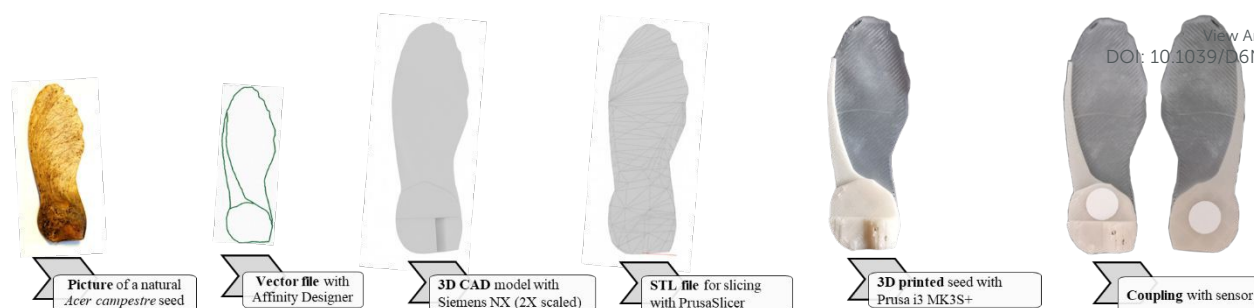


**Fig. 5** Development of the artificial seeds starting from the natural *Acer campestre* species. The flowchart consists of (i) the picture of natural *Acer campestre*, (ii) vector file extract from the contours, (iii) creation of 2x scaled CAD files, (iv) creation of 2x scaled STL files, (v) 3D printing of 2x scaled artificial *Acer campestre* using PHA, and (vi) integration of the fluorescent nanocomposite using ethyl cyanoacrylate as glue.

by  $\text{Er}^{3+}$  to emit green and/or red. Finally, the filling ratio is large enough that relevant wavelength-dependent scattering may occur despite the dispersed state of the nanoparticles in the polymer matrix, introducing additional non-linearity.

The thermometric performance of the mixed composites was evaluated between 268 K and 313 K. Fig. S7 (SI) shows the integrated blue (450 nm to 500 nm), green (520 nm to 570 nm) and red emissions (from 620 nm to 680 nm) as a function of temperature. The intensity responses to temperature were non-linear in general. The intensity of the green emissions from "50% Red, 50% Green" mixed emitters (hereafter green/red) increased by nearly 5% and then continuously dropped (Fig. 4A). Similar trend was detected also for the green/blue mixed emitters (Fig. S7, SI). For the mixture of blue and red emitters, a more linear decrease was detected (Fig. S7, SI). These non-linear trends are expected due to the spectral overlaps of the activators, as explained above.

We defined thermometric parameters  $\Delta_i$  as the ratios between the integral intensities of the blue vs. green ( $\Delta_1$ ), blue vs. red ( $\Delta_2$ ) and green vs. red ( $\Delta_3$ ) bands (Section S2 and Table S2, SI). These ratios are based on energy levels that arise from different emitting ions embedded into different hosts and have  $\Delta E$  above  $2000 \text{ cm}^{-1}$ ,<sup>30</sup> i.e. they are non-thermally coupled levels (NTCLs). Their temperature dependencies are commonly described using empirical polynomials.<sup>30</sup> All experimental  $\Delta_i$  for the NTCLs were thus fitted to the following equation:

$$\Delta_i = \frac{a_i + b_i T}{1 + c_i T + d_i T^2} \quad (4)$$

where  $a_i$ ,  $b_i$ ,  $c_i$ , and  $d_i$  are empirical constants. The thermometric performance of the mixed composites was evaluated by calculating the figures of merit  $S_{rel}$ , the temperature resolution  $\delta T$  and the repeatability  $R$  using Equations S6, S7, S8, respectively (Section S2, SI).<sup>2,3</sup>

The intensity ratios of all three mixed nanocomposites decreased with increasing temperature (Fig. 4B). The drop of the intensity ratio was largest for blue/green composites ( $\Delta_1$ , symbols in purple in Fig. 4B). The composite formed from  $\Delta_1$ , achieved a high value of  $S_{rel}$  (Equation S6, SI) in the range of  $33.9 \pm 1.3\% \text{ K}^{-1}$  at 268 K (Fig. 4C). The green/red ( $\Delta_3$ ) composites (grey line) had  $S_{rel}$  around  $32.5 \pm 1.6\% \text{ K}^{-1}$  at the same temperature. The composite formed from the blue and red ( $\Delta_2$ )

emitters (yellow line), displayed the lowest value of  $S_{rel}$  of approximately  $16.5 \pm 1.7\% \text{ K}^{-1}$  (Fig. 4C).

The temperature resolution,  $\delta T$ , indicates the lowest temperature change that a thermometer can resolve.<sup>2,3</sup>  $\delta T$  is inversely proportional to  $S_{rel}$  and proportional to the relative uncertainty of the intensity ratio (Equation S7, SI). Its values for  $\Delta_1$ ,  $\Delta_2$  and  $\Delta_3$  nanocomposites were 0.014 K, 0.030 K, and 0.015 K at 268 K, respectively. Blue/green composites provided the smallest resolution, mainly due to their high  $S_{rel}$  (Equation S7, SI). Thus, our mixed emitter composites reach temperature resolutions that are approximately 10 to 20-fold higher compared to state of the art based thermometers.<sup>15,31</sup>

The repeatability  $R$  indicates the ability of a thermometer to provide the same temperature measurement at different times under identical conditions.<sup>2,3</sup> It is commonly estimated by comparing readings during repeated heating/cooling cycles and calculating the values of  $\Delta$  or  $S_{rel}$ . Equation S8 (SI) indicated an  $R$  in the range between 96-98% during 5 cycles (Fig. S8, SI and Table S1, SI with a summary on the fitting parameters,  $S_{rel}$ ,  $\delta T$  and  $R$  for these mixed composites). State of the art thermometers achieve similar values of  $R$ ,<sup>15,31</sup> although not all reports contain quantitative data.

In the following, we compare the performances of different mixed emitter nanocomposites and the state of the art using  $S_{rel}$  because it is a widely applied figure of merit independent of operating wavelengths, acquisition setup or nature of the materials employed as thermometers.<sup>2,3</sup>

The maximal  $S_{rel}$  of our mixed emitters were approximately 40 times those of green  $\text{Er}^{3+}$ ,  $\text{Yb}^{3+}$  in  $\text{NaYF}_4$ ,<sup>32</sup> or in  $\text{NaY}(\text{WO}_4)_2$  emitters,<sup>33</sup> in exiting TCL thermometers (Fig. S9, SI). They were 70 times higher than those of blue emitters with  $\text{Tm}^{3+}$ ,  $\text{Yb}^{3+}$  in  $\text{NaLuF}_4$ ,<sup>34</sup> or in  $\text{Y}_2\text{O}_3$ ,<sup>35</sup> and 6 times than those of red ( $\text{Tm}^{3+}$  in  $\text{NaYb}(\text{MoO}_4)_2$ ,<sup>36</sup>) and NIR ( $\text{Nd}^{3+}$  in  $\text{LaF}_3$ ) emitters.<sup>37</sup>

The relative thermal sensitivities of state of the art NTCL based thermometers with blue  $\text{Tm}^{3+}$  in  $\text{NaGdF}_4@ \text{NaYF}_4$  and green emitting  $\text{Er}^{3+}$  in  $\text{NaYF}_4$  in a poly(methyl methacrylate) (PMMA) matrix,<sup>38</sup> or when codoped in molybdate hosts,<sup>39</sup> have  $S_{rel}$  of up to  $5.88\% \text{ K}^{-1}$  at 339 K (turquoise lines, Fig. 4D), approximately 5 to 6 times below our mixed emitters. A high  $S_{rel}$  of  $36.2\% \text{ K}^{-1}$  at 303 K was recorded when the blue emission (474 nm) and deep red emission (696 nm) of  $\text{Tm}^{3+}$  were combined in a  $\text{NaLaTi}_2\text{O}_6$  host,<sup>40</sup> (turquoise lines, Fig. 4D).



NTCLs based on core@shell nanoparticles emitting at different wavelength regions with emissions in the Vis and NIR regions

expansion coefficient to trigger Vis emissions with quench “on” properties. In this contribution, we limited ourselves to mixed

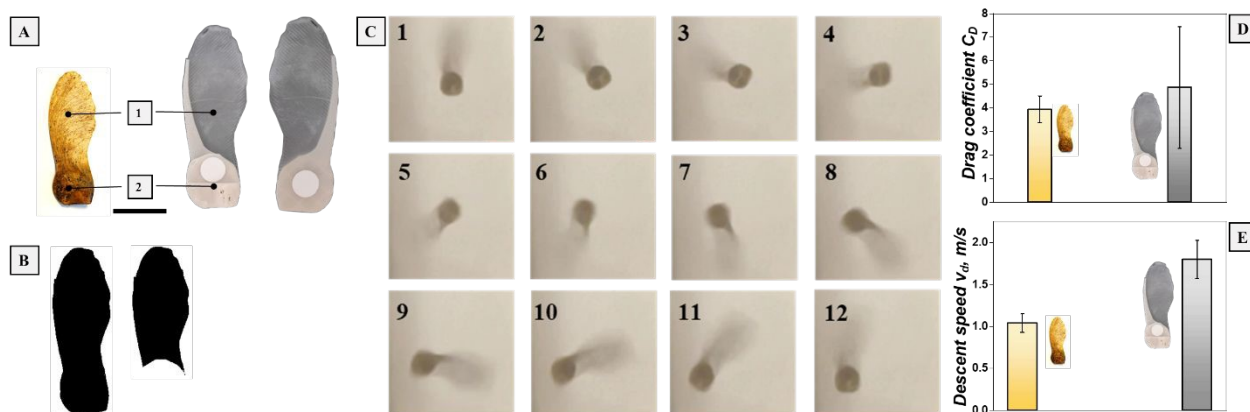


**Fig. 6** Morphometric and aerodynamic characterizations of natural and artificial *Acer campestre* seeds. (A) Natural *Acer campestre* seed composed of a capsule and a wing (under “1”) and a wing (under “2”). (B) Image binarization of the complete seed and of the wing for estimation of the wing surface ( $S$ ) and the wing loading ( $W/S$ ). (C) Twelve frames of the descent of the sensing seed for measuring the rotational velocity. Comparison of: (D) the drag coefficient ( $C_D$ ) and (E) the descent speed ( $v_d$ ) of the natural and the artificial seeds.

(turquoise line, Fig. 4D) have been introduced. An active core@inert shell  $\text{Yb}^{3+}:\text{NaErF}_4@\text{NaYF}_4$  nanostructure achieved an  $S_{rel}$  of 3.76%  $\text{K}^{-1}$  at 295 K by using the NTCLs of  $\text{Er}^{3+}$  at 540 nm and 1527 nm.<sup>41</sup> An even more complex single structure (an active core@inert shell@active shell  $\text{Er}^{3+}, \text{Yb}^{3+}:\text{NaYF}_4@\text{NaYF}_4@\text{NaYF}_4:\text{Yb}^{3+}, \text{Nd}^{3+}$ ) was used as a thermal probe based on the quench “on” of the red emission of  $\text{Er}^{3+}$  (654 nm) and quench “off” of the NIR emission of  $\text{Nd}^{3+}$  (803 nm).<sup>31</sup> These opposite trends led to  $S_{rel}$  of 9.6%  $\text{K}^{-1}$  at 303 K.<sup>31</sup> Recently, two different materials with quench “off” and “on” properties, were embedded within a hydrogel.<sup>15</sup> Quench “off” was assigned to the emission of  $\text{Er}^{3+}$  (540 nm) within  $\text{Er}^{3+}, \text{Yb}^{3+}:\text{NaYF}_4@\text{NaYF}_4$  nanostructures. Quench “on” was due to the emission of either  $\text{Nd}^{3+}$  (799 nm) or  $\text{Tm}^{3+}$  (796 nm) doped within 3  $\mu\text{m}$   $\text{Yb}_2\text{W}_3\text{O}_{12}$  microparticles. The ratio among  $\text{Er}^{3+}$  and  $\text{Nd}^{3+}$  achieved a maximum  $S_{rel}$  of 15.3%  $\text{K}^{-1}$  at 553 K. A boost in  $S_{rel}$  was achieved (23.84%  $\text{K}^{-1}$  at 380 K) for the ratio among  $\text{Er}^{3+}$  (540 nm) and  $\text{Tm}^{3+}$  (796 nm) (turquoise lines, Fig. 4D).<sup>15</sup>

Despite these high values of  $S_{rel}$  in the state of the art, our mixed emitter thermometers based on  $\Delta_1$  (purple line, Fig. 4D) and  $\Delta_3$  (gray line, Fig. 4D) are more sensitive (turquoise lines, Fig. 4D). Furthermore, our thermometers do not require complex core@shell particle architectures that are harder to optimize in terms of dopants (either sensitizers or activators). The NTCL thermometers described above require concurrent Vis/NIR optics to be properly readout. Our mixed emitter nanocomposites are fully operative within Vis range of spectrum. In addition, detectors such as silicon photodiodes and CCD or CMOS cameras for Vis are cheaper compared to InGaAs detectors for NIR light.<sup>42</sup>

A current limitation of our mixed emitter concept is the temperature range with high  $S_{rel}$  (268 K to 290 K): the sensitivity drops to 0.05%  $\text{K}^{-1}$  to 1%  $\text{K}^{-1}$  above 300 K (Fig. 4C, D). This temperature range can be extended by combining more than two emitters or designing hosts with a negative thermal

emitter composites for maximal sensitivity in the environmental temperature range because we were primarily interested in their application for environmental sensing.

We evaluate the application of the mixed emitters as sensitive elements in environmental probes. Current technologies for environmental sensing rely on complex materials that generate e-waste.<sup>43</sup> Recently, self-deployable and biocompatible artificial seeds inspired by plants, are growing as alternative probes.<sup>18, 19, 44</sup> These seeds mimic the properties of the natural plants. They react optically to environmental parameters and are read using drones equipped with fluorescence light detection and ranging (FLIDAR) technology placed on a distance. The artificial seeds can remain in the field where they degrade and cause no harm.<sup>18, 19, 44</sup>

It has been shown previously that passive fliers can be designed by creating artificial seeds inspired by natural *Acer campestre* (or samara). These seeds fly with the wind and are able to cover large distances and areas.<sup>45</sup> Artificial and fluorescent *Acer campestre* seeds (or fliers) have previously been produced via 3D printing technologies to monitor the temperature of topsoil.<sup>18</sup> The whole body of the artificial seed was constructed on commercial lanthanide doped particles (approximately 3  $\mu\text{m}$  in size).<sup>18</sup> The temperature of the topsoil was deduced based on the TCLs of  $\text{Er}^{3+}$  ions at 520 nm and 540 nm.<sup>18</sup> The single emitter composites used in these seeds had a limited  $S_{rel}$  however, which limited the distance between probe and optical reader. In practice, it made it necessary to fly a drone closely to the seed to record photoluminescence with sufficient SNRs for the analysis of the two green bands, which is difficult. Here, we address these limitations by 3D printing artificial *Acer campestre* seeds and attach into them the mixed emitter nanocomposites with high SNR and high  $S_{rel}$ .

Starting from the images of the natural *Acer campestre* seeds (Fig. 5), we drew a vectorized contour, followed by creating a vector file of the contours (Fig. 5). Then, a 3D CAD model was developed for the design of the artificial samara seeds. The CAD



model was converted into a STL format and sliced. A model was extruded and scaled up to 2x of the original dimensions of the natural seeds with the goal of allowing for a large area for coupling with the fluorescent sensors (Fig. 5). The artificial seeds were printed using PHA as a polymer. The fluorescent nanocomposite was coupled at both sides of the printed *Acer campestre* seed using ethyl cyanoacrylate as a glue. The morphometric and aerodynamic characteristics of the unit (the seed and fluorescent nanocomposite) were analyzed.

*Acer campestre* seeds are composed of a pericarp (marked with "1" in Fig. 6A) and a wing (marked with "2" in Fig. 6A). The morphological and physical characteristics of the natural seeds were measured to guide the process of printing the artificial seeds (Fig. S10, SI).<sup>18</sup> In short, the average mass was  $56 \pm 11$  mg (from 10 seeds). The average value of the wing surface ( $S$ ), estimated from wing image binarization, was  $173 \pm 21$  mm<sup>2</sup>. The wing loading ( $W/S$ ), with a weight ( $W$ ) of  $0.549 \pm 0.1 \times 10^{-3}$  N was  $3.17 \pm 1.01$  N/m<sup>2</sup>. In terms of their aerodynamic, the lab descent speed ( $v_d$ ), rotational velocity ( $\Omega$ ), wing tip speed ( $v_t$ ) and Drag coefficient ( $C_D$ ), were  $1.04 \pm 0.11$  m/s,  $160.5 \pm 23.3$  rad/s,  $3.94 \pm 0.57$  m/s, and  $4.87 \pm 2.58$  respectively, in accordance with our previous results.<sup>24, 25</sup>

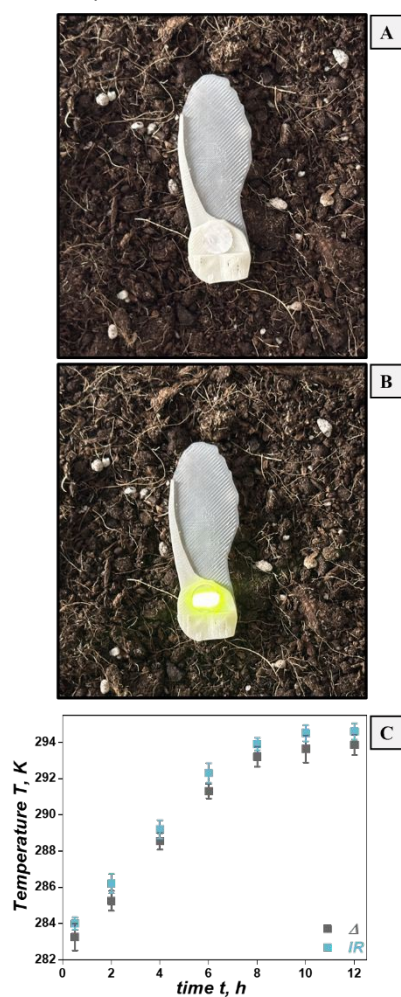


**Fig. 7** Monitoring the surface temperature of topsoil with the fluorescent artificial seeds: (A) on topsoil, (B) irradiated with 980 nm laser, and (C) temperature of the topsoil determined from the fluorescent seeds ("Δ" in gray) and from a reference external infrared thermometer ("IR" in blue).

The total mass ( $m$ ) of the flier with the artificial seed and the sensing unit was  $703.1 \pm 9.3$  mg and the mean  $W/S$  was  $709 \pm 9.1$  mm<sup>2</sup> (Fig. 6B).  $W/S$  of the printed flier was  $9.72 \pm 0.55$  N/m<sup>2</sup>, while  $\Omega$  (Fig. 6C),  $v_t$  and  $C_D$  were respectively  $144.1 \pm 15.3$  rad/s (Movie S1, SI),  $7.00 \pm 0.79$  m/s, and  $4.99 \pm 1.53$ , respectively. Both  $v_t$  and  $C_D$  values resulted statistically equal for natural and artificial seeds (Fig. 6D), as  $v_d$  of the artificial fliers was  $1.80 \pm 0.23$  m/s, approximately 80% more than the natural level (Fig. 6E), consistent with a more than 10-fold increase in mass. All results (Table S2, SI) imply the potential to print fluorescent artificial seeds that mimic the properties of the natural seeds by preserving the same design, regardless of the weight, dimensions and addition of the fluorescent nanocomposites. After integrating the fluorescent sensors into the artificial seeds, we conducted a proof-of-concept experiment. A distributed environmental sensing scenario was emulated by monitoring the surface temperature of topsoil with a printed fluorescent artificial seed. A freshly collected soil sample was placed on a flat surface (Fig. 7A). The seed with a fluorescent composite containing green/red mixture was placed on top. These emitters have a higher quantum yields compared to the blue nanoparticles. The seed was irradiated with a 980 nm laser (power density  $0.4$  W/cm<sup>2</sup>) using a custom-built optical setup to guide the beam perpendicular to the position of the fluorescent composite on the seed. The distance between the laser and the fluorescent seed was approximately 150 cm. Its lime-coloured emission (Fig. 7B) was recorded by a high-resolution Ocean Optics spectrometer (HB2000+) coupled with a flexible 400 μm diameter fiber. The soil was collected at low temperature in the morning (approximately 280 K) that slowly increased to room temperature within the controlled environment of a laboratory (295 K). The temperature of the topsoil was monitored using a reference external infrared thermometer ("IR", Fig. 7C).

The fluorescent seed was continuously irradiated with the NIR laser for a total of 12 hours, and the thermometric parameter  $\Delta$  was calculated using the ratio among the green and red bands as in  $\Delta_3$  and averaged in 10 min intervals. Based on the calibration curve of  $\Delta_3$ , the topsoil temperatures were calculated ("Δ", Fig. 7C). The mean differences between optical thermometry and IR camera were 0.5 K to 0.8 K after 5 repetitions of the experiment (Fig. 7C). Part of this is due to the low thermal conductivity of the PHA polymer ( $0.10$  W·m<sup>-1</sup>·K<sup>-1</sup> to  $0.25$  W·m<sup>-1</sup>·K<sup>-1</sup>),<sup>46</sup> that leads to a slow heat transfer. This result indicates that fluorescent artificial fliers are a suitable platform for monitoring the surface temperature of topsoil within narrow environmental range and can be applied for outdoor sensing with drones equipped with FLIDAR (Movie S2, SI).

## Conclusions

In summary, we demonstrated that bright upconverting nanocomposites can be used to create plant-inspired artificial fliers that act as sensitive thermometers to monitor the surface temperature of topsoil. The nanocomposites were based on



red, green and blue upconverting emitters and biodegradable PHA polymer. By mixing the emitters, we created fluorescent nanocomposites with clearly distinguishable emission signals, high SNRs and  $S_{rel}$  up to 34%  $K^{-1}$ , overcoming current limitations of the state-of-the-art thermometers. Integrating these thermometers into the artificial fliers confirmed that they are suitable for environmental monitoring.

The artificial seeds created here have mixed emitter nanocomposites attached on the pericarp. It is also possible to make artificial fliers entirely out of the fluorescent nanoparticles, for example by direct ink writing and density reduction with a leaching process,<sup>44</sup> or by using lightweight aerogels that are formed via freeze-drying.<sup>47</sup>

The mixed emitter nanocomposites that we introduced here are designed for environmental temperatures and limited in their operational range. The concept is more versatile: combinations with more than two emitters and with particles that have thermal quench “on” and quench “off” properties are possible to extend and tune their temperature range.

## Author contributions

Albenc Nexha and Stefano Mariani wrote the original draft of the manuscript. Albenc Nexha and Anja Colbus performed the experiments on the upconverting nanoparticles, preparation of the composites and luminescence thermometry. Stefano Mariani and Kliton Cikalleshi worked on the production and characterization of the artificial seeds. All authors took part in the conceptualization, reviewing, and editing of the manuscript. Barbara Mazzolai and Tobias Kraus led the supervision and funding acquisition.

## Conflicts of interest

There are no conflicts to declare.

## Data availability

The data that support the findings of this study will be made available upon request from the corresponding authors.

## Acknowledgements

This project has received funding from the European Union’s Horizon 2020 research and innovation programme under grant agreement No. 101017940 (I-Seed).

## References

- G. Chen, H. Qiu, P. N. Prasad and X. Chen, *Chem. Rev.* 2014, **114**, 5161-5214.
- A. Nexha, J. J. Carvajal, M. C. Pujol, F. Díaz and M. Aguiló, *Nanoscale* 2021, **13**, 7913-7987.
- A. Nexha, M. C. Pujol Baiges and J. J. Carvajal Martí, in *Luminescent Thermometry: Applications and Uses*, eds. J. J. Carvajal Martí and M. C. Pujol Baiges, Springer International Publishing, Cham, 2023, DOI:10.1007/978-3-031-28516-5\_6, pp. 221-268.
- H. Suo, X. Zhao, Z. Zhang, Y. Wang, J. Sun, M. Jin and C. Guo, *Laser Photonics Rev.* 2021, **15**, 2000319.
- M. L. Debasu, D. Ananias, I. Pastoriza-Santos, L. M. Liz-Marzán, J. Rocha and L. D. Carlos, *Adv. Mater.* 2013, **25**, 4868-4874.
- O. A. Savchuk, J. J. Carvajal, M. C. Pujol, E. W. Barrera, J. Massons, M. Aguilo and F. Diaz, *J. Phys. Chem. C* 2015, **119**, 18546-18558.
- M. Suta, Ž. Antić, V. Đorđević, S. Kuzman, M. D. Dramićanin and A. Meijerink, *Nanomaterials* 2020, **10**, 543.
- C. D. S. Brites, P. P. Lima, N. J. O. Silva, A. Millán, V. S. Amaral, F. Palacio and L. D. Carlos, *Adv. Mater.* 2010, **22**, 4499-4504.
- Y. H. Han, C. B. Tian, Q. H. Li and S. W. Du, *J. Mater. Chem. C* 2014, **2**, 8065-8070.
- S. Zheng, W. Chen, D. Tan, J. Zhou, Q. Guo, W. Jiang, C. Xu, X. Liu and J. Qiu, *Nanoscale* 2014, **6**, 5675-5679.
- A. Nexha, J. J. Carvajal, M. C. Pujol, F. Díaz and M. Aguiló, *J. Mater. Chem. C* 2021, **9**, 2024-2036.
- O. A. Savchuk, J. J. Carvajal, C. D. S. Brites, L. D. Carlos, M. Aguilo and F. Diaz, *Nanoscale* 2018, **10**, 6602-6610.
- T. Y. Sun, D. Q. Zhang, X. F. Yu, Y. Xiang, M. Luo, J. H. Wang, G. L. Tan, Q. Q. Wang and P. K. Chu, *Nanoscale* 2013, **5**, 1629-1637.
- E. N. Cerón, D. H. Ortgies, B. del Rosal, F. Ren, A. Benayas, F. Vetrone, D. Ma, F. Sanz-Rodríguez, J. G. Solé, D. Jaque and E. M. Rodríguez, *Adv. Mater.* 2015, **27**, 4781-4787.
- Y. Wang, L. Lei, R. Ye, G. Jia, Y. Hua, D. Deng and S. Xu, *ACS Appl. Mater. Interfaces* 2021, **13**, 23951-23959.
- H. Park, H. He, X. Yan, X. Liu, N. S. Scrutton and G.-Q. Chen, *Biotechnol. Adv.* 2024, **71**, 108320.
- M. Fernandes, A. Salvador, M. M. Alves and A. A. Vicente, *Polym. Degrad. Stab.* 2020, **182**, 109408.
- K. Cikalleshi, A. Nexha, T. Kister, M. Ronzan, A. Mondini, S. Mariani, T. Kraus and B. Mazzolai, *Sci. Adv.* 2023, **9**, eadi8492.
- A. Nexha, S. Mariani, K. Cikalleshi, T. Kister, B. Mazzolai and T. Kraus, *Nanoscale* 2025, **17**, 18143-18152.
- M. Mo, Y. Liwen, R. Guozhong, X. Changfu, L. Jianguo and Y. Qibin, *J. Lumin.* 2011, **131**, 1482-1486.
- G. Tian, Z. Gu, L. Zhou, W. Yin, X. Liu, L. Yan, S. Jin, W. Ren, G. Xing, S. Li and Y. Zhao, *Adv. Mater.* 2012, **24**, 1226-1231.
- G. Wang, Q. Peng and Y. Li, *J. Am. Chem. Soc.* 2009, **131**, 14200-14201.
- C. A. Schneider, W. S. Rasband and K. W. Eliceiri, *Nat. Methods* 2012, **9**, 671-675.
- S. J. Lee, E. J. Lee and M. H. Sohn, *Exp. Fluids* 2014, **55**, 1718.
- G. K. Nave, N. Hall, K. Somers, B. Davis, H. Gruszewski, C. Powers, M. Collver, D. G. Schmale and S. D. Ross, *Biomimetics* 2021, **6**, 23.
- B. V. N. Kumar and R. E. Kroon, *Opt. Mater.* 2025, **167**, 117274.
- A. S. Nizamutdinov, A. A. Shavelev, A. V. Astrakhantseva, K. N. Boldyrev, A. G. Nikolaev, E. B. Dunina, A. A. Kornienko, A. A. Pynenkov, A. A. Lyapin, S. V. Kuznetsov and V. V. Semashko, *Opt. Mater.* 2024, **147**, 114585.
- H. Xia, J. Feng, Y. Wang, J. Li, Z. Jia and C. Tu, *Sci. Rep.* 2015, **5**, 13988.



29. R. T. Wegh, A. Meijerink, R. J. Lamminmäki and H. Jorma, *J. Lumin.* 2000, **87-89**, 1002-1004.
30. G. Xiang, Y. Yi, Z. Yang, Y. Wang, L. Yao, S. Jiang, X. Zhou, L. Li, X. Wang and J. Zhang, *Inorg. Chem. Front.* 2024, **11**, 1522-1530.
31. C. Mi, J. Zhou, F. Wang, G. Lin and D. Jin, *Chem. Mater.* 2019, **31**, 9480-9487.
32. L. Li, F. Qin, Y. Zhou, Y. Zheng, H. Zhao and Z. Zhang, *ACS Appl. Nano Mater.* 2018, **1**, 1912-1920.
33. M. Lin, L. Xie, Z. Wang, B. S. Richards, G. Gao and J. Zhong, *J. Mater. Chem. C* 2019, **7**, 2971-2977.
34. H. Lu, H. Hao, G. Shi, Y. Gao, R. Wang, Y. Song, Y. Wang and X. Zhang, *RSC Adv.* 2016, **6**, 55307-55311.
35. G. Chen, R. Lei, F. Huang, H. Wang, S. Zhao and S. Xu, *Luminescence* 2018, **33**, 1262-1267.
36. M. Jia, Z. Sun, H. Xu, X. Jin, Z. Lv, T. Sheng and Z. Fu, *J. Mater. Chem. C* 2020, **8**, 15603-15608.
37. E. Carrasco, B. del Rosal, F. Sanz-Rodríguez, Á. J. de la Fuente, P. H. Gonzalez, U. Rocha, K. U. Kumar, C. Jacinto, J. G. Solé and D. Jaque, *Adv. Funct. Mater.* 2015, **25**, 615-626.
38. E. D. Martínez, C. D. S. Brites, L. D. Carlos, A. F. García-Flores, R. R. Urbano and C. Rettori, *Adv. Funct. Mater.* 2019, **29**, 1807758.
39. Z. Zhang, D. Zhu, Z. Huang, Z. Zhu, J. Liu and K. Li, *Mater. Today Chem.* 2025, **48**, 102971.
40. K. Li, Z. Zhang, D. Zhu and C. Yue, *Inorg. Chem. Front.* 2024, **11**, 7464-7474.
41. Y. Wang, L. Lei, E. Liu, Y. Cheng and S. Xu, *Chem. Commun.* 2021, **57**, 9092-9095.
42. B. Zhu and H. Jonathan, *Sensors* 2024, **24**, 3539.
43. R. Ouni and K. Saleem, *Sustainability* 2022, **14**, 8356.
44. S. Mariani, K. Cikallesi, M. Ronzan, C. Filippeschi, G. A. Naselli and B. Mazzolai, *Small* 2025, **21**, 2403582.
45. K. Yasuda and A. Azuma, *J. Theor. Biol.* 1997, **185**, 313-320.
46. X. Liang, D. K. Cha and Q. Xie, *Resour. Conserv. Recycl. Adv.* 2024, **21**, 200206.
47. G. Gallo, R. Tu, C. Filippeschi, S. Mariani and B. Mazzolai, *Adv. Sci.* 2026, **13**, e08949.

View Article Online  
DOI: 10.1039/D6NR00489J



**Data Availability Statement**

View Article Online  
DOI: 10.1039/D6NR00489J

The data that support the findings of this study will be made available upon request from the corresponding authors.

